Spray Coating Experiments: Setups and Methodologies

13 Thin Films III

Spray Coating Experiments: Setups and Methodologies

EVIDENT OLYMPUS

WILEY

The latest eBook from Advanced Optical Metrology. Download for free.

Spray Coating Experiments: Setups and Methodologies, is the third in our Thin Films eBook series. This publication provides an introduction to spray coating, three article digests from Wiley Online Library and the latest news about Evident's Image of the Year Award 2022.

Wiley in collaboration with Evident, are committed to bridging the gap between fundamental research and industrial applications in the field of optical metrology. We strive to do this by collecting and organizing existing information, making it more accessible and useful for researchers and practitioners alike.

EVIDENT OLYMPUS

WILEY

Temperature-Controlled Pathway Complexity in Self-Assembly of Perylene Diimide-Polydiacetylene Supramolecule

Joonsik Seo, Mohammed Iqbal Khazi, Kwangmin Bae, and Jong-Man Kim*

Self-assembly process represents one of the most powerful and efficient methods for designing functional nanomaterials. For generating optimal functional materials, understanding the pathway complexity during self-assembly is essential, which involves the aggregation of molecules into thermodynamically or kinetically favored pathways. Herein, a functional perylene diimide (PDI) derivative by introducing diacetylene (DA) chains (PDI-DA) is designed. Temperature control pathway complexity with the evolution of distinct morphology for the kinetic and thermodynamic product of PDI-DA is investigated in detail. A facile strategy of UV-induced polymerization is adopted to trap and capture metastable kinetic intermediates to understand the self-assembly mechanism. PDI-DA showed two kinetic intermediates having the morphology of nanosheets and nanoparticles before transforming into the thermodynamic product having fibrous morphology. Spectroscopic studies revealed the existence of distinct H- and J-aggregates for kinetic and thermodynamic products respectively. The polymerized fibrous PDI-DA displayed reversible switching between J-aggregate and H-aggregate.

1. Introduction

Supramolecular self-assembly is a powerful tool to design and construct functional materials with tailored properties through the hierarchical organization of the molecular building blocks.[1–5] Supramolecular self-assembly has created an opportunity to engineer a library of innovative multifunctional performance materials based on predictive molecular interactions, where various, typically nanometer-sized, objects with precisely engineered sizes, shapes, compositions, and dimensions can be constructed.[6–10] Weak directional molecular forces are central to self-assembly in general, for generating stable supramolecular structures and have been widely explored to develop new paradigms in material science ranging from optoelectronic materials to biomaterials.[11–14]

J. Seo, M. I. Khazi, K. Bae, J.-M. Kim
Department of Chemical Engineering
Hanyang University
Seoul 04763, Korea
E-mail: jmk@hanyang.ac.kr
J.-M. Kim
Institute of Nano Science and Technology
Hanyang University
Seoul 04763, Korea

The ORCID identification number(s) for the author(s) of this article can be found under https://doi.org/10.1002/smll.202206428.

To arrive at functional materials with optimal molecular organization, control over the self-assembly process is a prerequisite.[15–17] Since the molecular organization is a direct consequence of the pathways involved in the supramolecular assembly process, and often, multiple pathways are involved that compete for the same molecular building block, a phenomenon termed pathway complexity.[18–21] Molecular assembly process is widely considered to operate under thermodynamic control and thereby the possibility of kinetic processes that can also occur has been relatively less studied. Therefore, much more effort should be made to further excavate self-assembly mechanisms for understanding the relationship between thermodynamics and kinetics in self-assembly processes. In a key example of kinetically controlled supramolecular assembly, Meijer et al reported competing pathways and the difference between kinetic and thermodynamic pathways.[22,23] The recent advancement of analytical tools as well as the development of kinetic models and simulations have led to an increasing interest in understanding the relationship between thermodynamics and kinetics in self-assembly processes.[24–28]

π-Conjugated molecular systems have attracted increasing attention because of their interesting structure, optical and electronic properties to construct functional materials, and feasibility for device fabrications.[29–34] However, mechanistic information of the self-assembly of the π-conjugated system through π–π stacking interactions is still in a nascent stage. There are only selected examples of the kinetically controlled supramolecular assembly process, wherein aggregation proceeds through the formation of metastable species that are crucial for transforming into a stable thermodynamic product. Metastable products are reported to be embedded with more superior properties, and therefore the preparation protocol should be optimized to favor the metastable pathway instead of other competing pathways.

In the investigation described herein, we designed a π-electron rich molecular system by integrating perylene diimide (PDI) and diacetylene (DA), PDI-DA. The diacetylene template with strong π- π stacking characteristic assembles into a supermolecular structure which transforms into a highly π-conjugated polydiacetylene (PDA) upon UV-induced topochemical polymerization.[35–51] Detailed competing pathways for self-assembly and the influence for distinct morphological evolution has been

discussed. Surprisingly PDI-DA exhibited higher complexity in competing pathways with two kinetic products. Since the cross-linking of self-assembled diacetylenes into polymerized covalently connected PDA can be readily achieved by facile UV-irradiation, an approach to trap and identify kinetically favored metastable intermediates was utilized. The fibrous PDI-DA generated, following the thermodynamic aggregation pathway was polymerized by UV irradiation to generate purple phase PDA. More interestingly, polymerized PDI-DA fibers displayed the reversible thermochromic behavior with the transition between purple and red phases through a reversible conversion of J-aggregate and H-aggregate and at the same time, changes between intermolecular and intramolecular hydrogen bonding.

Considering the above results and among various approaches and possibilities to understand pathway complexity, the incorporation of a polymerizable DA template in a molecular design served as an efficient tool based on a photopolymerization strategy for "trapping" metastable intermediates to distinguish competing pathway complexity in molecular self-assembly. Since DA monomers can be easily transformed into covalently-linked robust polymeric structures, the supramolecular intermedii-

ates can be entrapped in different states which enables detection and studies of individual supramolecular transformation steps and provides valuable insight into the mechanism of self-assembly phenomena. Pathway complexity has been shown to be intimately linked to their morphology, the trap facilitated by photopolymerization is very useful to isolate stable intermediates to study structural morphology. Eventually, in the course of our investigation to demonstrate the potential of polymerizable DA templates to arrest the self-assembly process at the different stages, we discovered that it is possible to "catch" the kinetic intermediates, which are too fast to be monitored. The advantages of incorporating the DA templates are no doubt the important development that gives a facile and clear insight into sequential competing pathway complexity during the self-assembly process.

2. Results and Discussion

Amide-functionalized π-electron-rich PDI derivative (PDI-DA) bearing six photopolymerizable DA templates was designed and synthesized. As shown in **Scheme 1**, DA chains
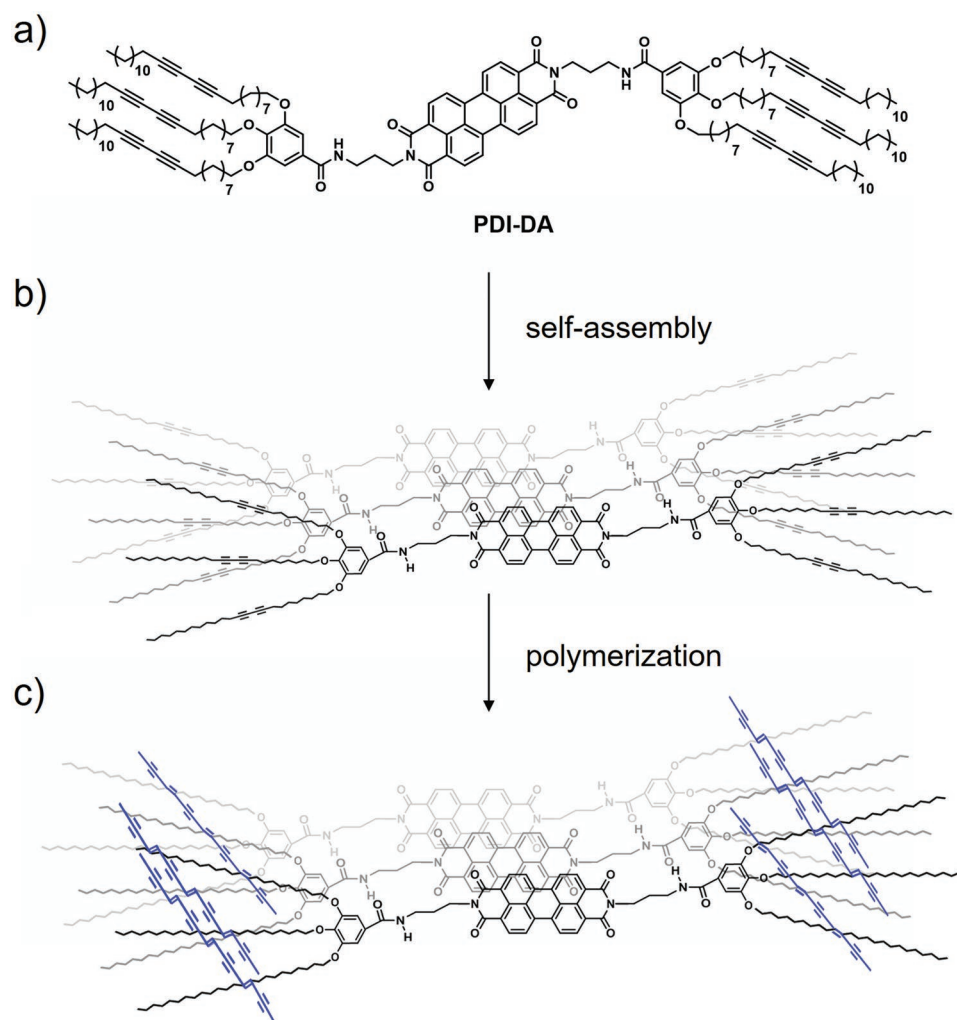
Scheme 1. Schematic illustration of self-assembly and polymerization of PDI-DA. a) Molecular structure of PDI-DA. b) Self-assembly of monomeric PDI-DA via intermolecular π-π stacking interactions. c) UV-induced topochemically polymerized PDI-DA having conjugated ene-yne bond.
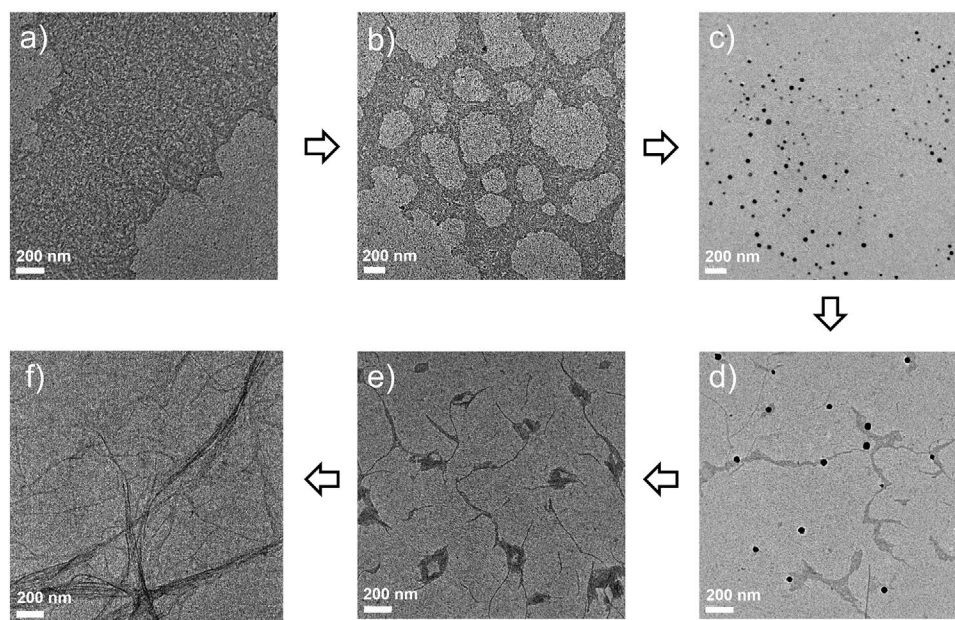
Figure 1. TEM images of morphological evolution and transformation during self-assembly process of PDI-DA. a) The initially formed nanosheets at 30 °C b) changes into irregular hole-like clusters on cooling at 20 °C and c) dissociate to form nanoparticles at 10 °C, d) which are transformed to intermediate and e) at standing time of 5 min and f) 10 min time duration and eventually transform into nanofibers after 150 min maintained at 10 °C.

are symmetrically located in the PDI-DA structure. The π-π stacking characteristic of the DA template and PDI, and complementary hydrogen bonding interactions of the amide linkage direct the DA chains to self-organize into optimal orientation for topochemical polymerization to form a robust covalently connected polymeric PDA structure. It has been reported by Würthner and coworkers that this type of molecule forms aggregates of various morphologies via intermolecular or intramolecular hydrogen bonding interactions.[52] For the synthesis of PDI-DA, a multistep protocol was employed involving imidization of perylene-3,4:9,10-tetracarboxylic acid bisanhydride with N-(3-aminopropyl)-3,4,5-tris(pentacosa-10,12-diyn-1-yloxy)benzamide in imidazole (see Scheme S1). All the synthesized products were characterized by analytical techniques and results were found in accordance with the formation of PDI-DA (see Figure S1–S3, Supporting Information).

The aggregation behavior for the self-assembly process was investigated in the toluene (Tol)/methylcyclohexane (MCH) solvent mixture in ratios at 1:3 (v/v). First, PDI-DA in the solvent mixture was heated to clarity and then cooled to 10 °C in a temperature-controlled cell to form self-assembled aggregates. This fabrication protocol results in the fast formation of metastable nanosheets, which then transform into nanoparticles and finally form fibrillar morphology. We first used transmission electron microscopy (TEM) to investigate the self-assembly process of PDI-DA. As shown in **Figure 1**a, drop cast deposition of ≈0.1 mL of PDI-DA in 1 mL MCH/Tol forms a metastable supramolecular nanosheet at 30 °C, which shows nanosheets spread over several micrometers (first kinetic product). The height profile of self-assembled nanosheets is measured by atomic force microscopy (AFM) analysis. AFM measurements of the heights of the nanosheets indicated a molecular ordering thickness of 7.25 nm, typical for flat-lying π-conjugated molecules (Figure S4,

Supporting Information). Supramolecular self-assembly of irregular hole-like clusters was triggered by post-cooling the sample to ≈20 °C for 10 min, wherein most of the molecules on the surface rearranged themselves from initial nanosheet morphology and dissociated into an irregular shape (Figure 1b). After attaining a further lower temperature of 10 °C, the second kinetic product of distinct nanoparticle morphology was observed (Figure 1c). As the self-assembly process proceeds at 10 °C, the kinetically favored nanoparticles gradually transformed into fibrillar structures, which are expected to be thermodynamically stable self-assembled structures (Figure 1d-f).

In addition to the interesting temperature-dependent morphological transformation of self-assembled structures, PDI-DA displayed distinct characteristic absorption spectral patterns during the self-assembly process for the kinetic and thermodynamic products. The formation of such interchanging aggregates has important consequences for the energies of the excited states and stable forms and can strongly modify optical absorption. This feature was probed by monitoring temperature-dependent and time-dependent absorption spectroscopy. The formation of metastable nanosheets and nanoparticles was studied by monitoring temperature-dependent UV-vis spectra of a solvent mixture of Tol/MCH (1:3, v/v) at a cooling rate of 5 °C min^{-1}. As shown in Periodicala, supramolecular polymerization proceeds as the temperature decreases, and the absorption spectrum recorded at 10 °C displays the typical spectral feature of H-aggregates. It could be expected that nanosheets and nanoparticles are H-aggregates. Interestingly, time-dependent absorption spectroscopy (**Figure 2**b) shows the transformation of the H-aggregates (nanoparticles) into the J-aggregates (nanofibril). The TEM images (Figure 1) and absorption spectra (Figure 2b) clearly explain that the initially formed nanosheets change into nanoparticles, the second intermediates during the cooling process, and
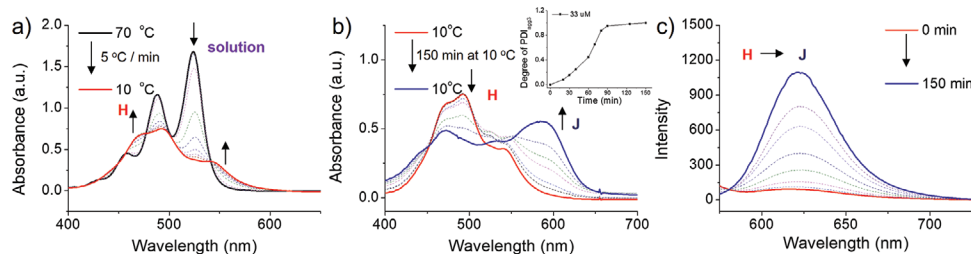
Figure 2. a) Temperature-dependent UV-vis absorption spectra ($c_t = 33 \times 10^{-6}$ M) in Tol/MCH (1:3, v/v). b–c) Time-dependent absorption (b) and emission (c) spectra of spontaneous transformation of the H-aggregate into J-aggregate at 10 °C. Insets (b): Plot of the degree of PDI-DAagg III calculated from the apparent absorption coefficients at $\lambda = 587$ nm observed in the transformation process from PDI-DAagg II to PDI-DAagg III at 10 °C. In (b) absorption spectrum was recorded at 0 min at 10 °C (red line) and after 150 min maintained at 10 °C (blue line). In (c) at 0 min (red line) and after 150 min (blue line).

finally transform into thermodynamically stable nanofibers over time with changes in the intermolecular stacking arrangements. At a cooling temperature of 10 °C, the nanoparticle-to-nanofibril conversion process in the aggregates solution was also analyzed by using a degree of PDI aggregation (α_{agg}) calculated from the apparent absorption coefficients ($\lambda = 587$ nm). Surprisingly, it is a unique case to change into a thermodynamically stable form after interchanging through two kinetic intermediates. Hence, it is likely that the early stage is dominated by kinetic aggregation which transforms into a thermodynamically stable product. The morphological transition was also confirmed in the emission spectroscopy. The fluorescence intensity increases as nanoparticles changes to nanofibrils, which is the typical characteristic of H- and J-aggregates (Figure 2c).

Temperature-dependent spectra were monitored at various concentrations between 8 to 66 µM to determine the thermodynamic parameters of each aggregate in supramolecular polymerization. The temperature-dependent degree of aggregation (α_{agg}) of nanoparticles and nanofibers was calculated for the cooling and heating process (**Figure 3**). For nanoparticles, the isodesmic model and cooperative model were applied, which reveals a nonsigmoidal transition and indicates the cooperative self-assembly mechanism (Figure 3a). The observed nonsigmoidal transitions were fitted by using the cooperative model (Figure S5, Supporting Information). The critical temperatures (T_e) and elongation enthalpy (ΔH_e) values of nanoparticles were calculated to be 35.1 to 54.4 °C and −51.6 to −56.3 kJ mol^{-1} respectively (Table S1, Supporting Information). On the other

hand, the critical temperatures (T_e) and elongation enthalpy (ΔH_e) values were calculated to be 63.45 to 66.25 °C and -101 to −126.8 kJ mol^{-1} respectively, which confirms that nano fibrillar morphology is the thermodynamic product (Figure 3b and Table S2, Supporting Information). These results indicate that nanoparticles are kinetically favored state and pathway complexity occurs during self-assembly. However, we could not able to analyze nanosheets because they quickly dissociated within a short time.

The amide functionality linked to the PDI core is expected to promote H-bonding driven π-stacking for the self-assembly of PDI-DA. The effect of hydrogen bonding on the stabilization of kinetically trapped states (nanosheets and nanoparticles) and thermodynamically stable states (nanofibers) was probed by Fourier transform infrared spectroscopy (FT-IR). The transformation from nanoparticle to nanofiber is accompanied by hydrogen bonding rearrangement of amide groups and PDI molecular stacking (Figure S6, Supporting Information). The broad N–H stretching band ≈3260–3400 cm^{-1} indicates intramolecular hydrogen bonds from amide NH to carbonyl oxygen in nanoparticles in H-aggregated PDI-DA. A new stretching band at 3270 cm^{-1} provides unequivocal evidence in support of intermolecular H-bonding among the amide groups of repetitive stacking units in

J-aggregated PDI-DA. This transformation leads to a further shift of the N–H stretching band to a lower frequency. Thus taking into account these observations, it is agreeable that the type of aggregation during the self-assembly process is directed
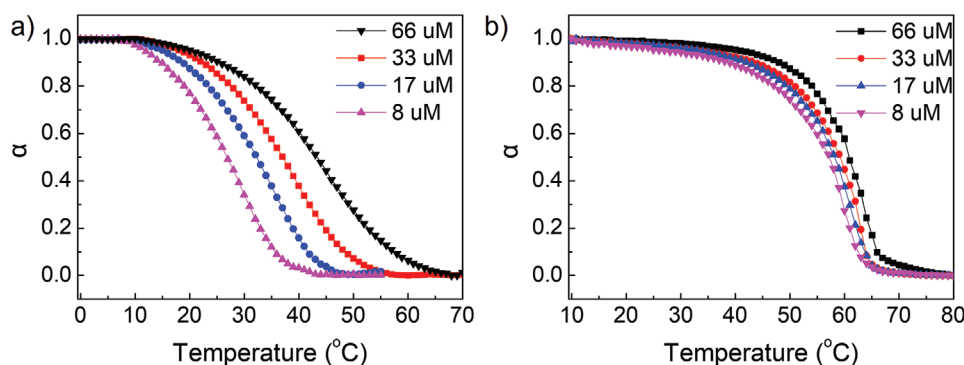

Figure 3. a,b) Plot of the faction of aggregates (α) as a function of temperature for H-aggregates (a) and J-aggregates (b) in Tol/MCH (1:3, v/v) at given concentrations (indicated above the respective curve). The α was calculated from the absorption at 523 nm (a) and at 587 nm (b).

ADVANCED
SCIENCE NEWS
www.advancedsciencenews.com

NANO · MICRO
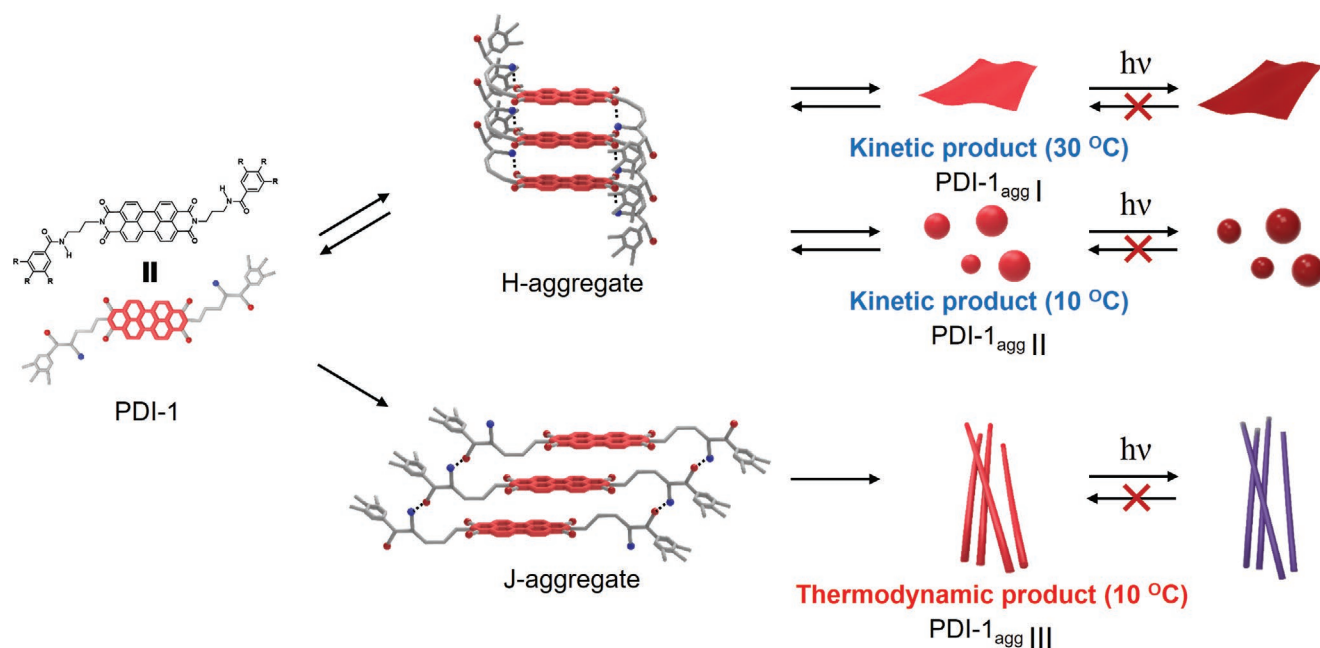**small**
www.small-journal.com

Figure 4. Schematic representation of aggregation pathway of PDI-DA into three aggregates and control of H- and J-aggregates by thermal treatment and UV irradiation. Self-assembly of PDI-DA is initiated by the formation of H-aggregate. A kinetically favored metastable PDI-DAagg I is formed in an initial nucleation step during the cooling process (65 °C to 30 °C). The initially formed nanosheet dissociate to develop into PDI-DAagg II (nanoparticle) during the cooling process (30 °C to 10 °C). UV irradiation to kinetic products promotes polymerization and stops further disassembly process. Without UV irradiation, PDI-DAagg II is slowly transformed into thermodynamically stable nanofibers. Polymerization of diacetylene units in three different PDI-DA aggregates affords covalent modification of polymorph nanostructures.

by synergistic H-bonding interactions and the growth happens in directions by combined H-bonding and π–π interactions.

On the basis of the collective spectroscopic and microscopic results as well as from our careful observation, we could speculate the possible reason behind the temperature-dependent morphological transformation. It is likely due to the rearrangement of the hydrogen bonding interaction pattern during the cooling process that eventually promotes distinct aggregation. The overall schematic representation of the aggregation pathway of PDI-DA is displayed in **Figure 4**. Interestingly, the existence of metastable nanosheets and nanoparticles indicates that the process of self-assembly of PDI-DA involves three different aggregation pathways that lead to the formation of kinetically favored nanosheets and nanoparticles, and thermodynamically favored nanofibers (Figures 1,4). The nanosheets and nanoparticles originated from intramolecular hydrogen-bonded H-aggregate, whereas the nanofibers originated from intermolecular hydrogen-bonded J-aggregate. Initially, during the self-assembly process, the solution of PDI-DA generates kinetically favored metastable nanosheets via initial nucleation during cooling. The UV-induced polymerization of the nanosheets promotes the cross-linking of the diacetylene template of adjacent DA units and of generates the kinetically-arrested polymeric nanosheet structures, which prevents the kinetically favored intermediates from dissociating to the original monomeric state. In the absence of trapping, the metastable nanosheets dissociate into monomers and form kinetically favored nanoparticles via a second aggregation pathway. Similar to nanosheets, UV-irradiation generates photopolymerization to form covalently trapped nanoparticles.

On the other hand, without UV irradiation, nanoparticles dissociate into monomers as described in Figure 4, and form thermodynamically stable nanofibers through a third aggregation pathway. To assess the photo-simulated trapping potential and stability of the trapped intermediates, UV light was irradiated to the PDI-DA solution at various stages of the self-assembly process. TEM imaging was performed to analyze the morphology of UV-light-induced trapped intermediates (Figure S7, Supporting Information). TEM images reveal that the UV-induced crosslinking forming a covalent PDA structure arrests the nanosheet and nanoparticle morphology corresponding to kinetic products, serving as a clamp to restrict structural dissociation into the fibrillar structure. Similar to the thermodynamic morphology of monomeric PDI-DA, the PDA form retains the fibrillar morphology with a highly robust structure.

The absorption spectra of PDI-DA in the Tol/MCH (1:3, v/v) solvent mixture were recorded after UV irradiation (**Figure 5**a,b). Since nanosheets are formed during the cooling process and dissociated rapidly, UV light was irradiated in a solution state. To form a polymerized nanosheet, the solution was placed on an ice pack and cooled to 10 °C, and later irradiated with UV light. Time-dependent morphological behavior for kinetic products after UV-induced polymerization was examined by using TEM spectroscopy. The red and blue lines in Figure 5a,b represent the absorption spectra of UV-irradiated nanosheet solution after 1 hour (red line) and 2 days (blue), respectively. As displayed in Figure 5a, no spectral change was observed for the heat-treated nanosheet solution to further transformation into the thermodynamic product and the dissociation of metastable nanosheets is supposedly stopped and arrested.
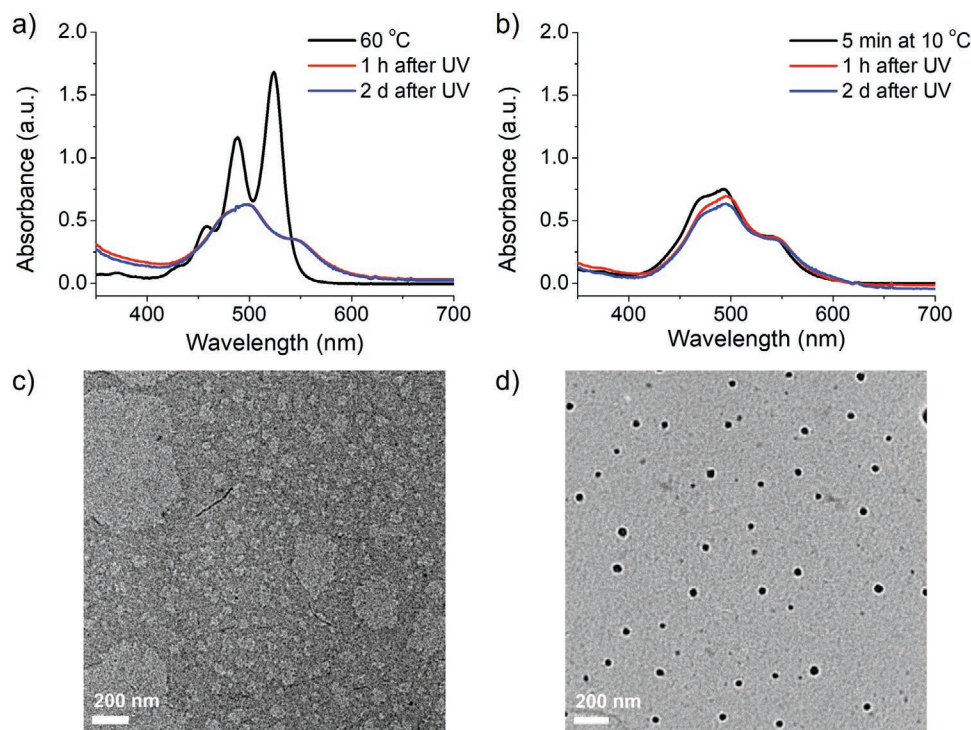
ADVANCED
SCIENCE NEWS

www.advancedsciencenews.com

NANO · MICRO

small
www.small-journal.com

Figure 5. a,b) Absorption spectra (ct = 33 × 10⁻⁶M) of polymerized nanosheets (a) and nanoparticles (b) in Tol/MCH (1:3, v/v). Black line represent the absorption spectra obtained before UV irradiation. Red and blue line represent the absorption spectra obtained after UV light irradiation (a, 5 mW cm⁻², 900 s), (b, 10 mW cm⁻², 200 s) followed by standing at 10 °C for 1 h (a, red line) and 24 h (b, blue line). c,d) TEM images obtained after 2 d of the UV-irradiated (254 nm, 20 mW cm⁻², 10 s) of PDI-DA aggregates solution containing nanosheets (c) and nanoparticles (d).

This mechanism of kinetic trapping in self-assembly is further evidenced by the TEM imaging. As shown in Figure 5c, metastable nanosheets retained their morphology intact even after standing for two days after UV exposure, suggesting effective covalent cross-linking induces the trapping of kinetic product. Similarly, polymerized kinetic controlled nanoparticles prepared by irradiating UV light into the aggregates following the cooling process at 10 °C do not show any spectral and morphological changes (Figure 5b), strongly suggesting covalently trapped nanoparticles are stable in aggregates solution for several days. Also, the red and blue lines in Figure 5b showed a nearly perfect overlapping spectral pattern for UV-irradiated nanoparticles solution after standing for 1 hour (red line) and 2 days (blue line) at 10 °C. Morphological stability of trapped nanoparticles was confirmed by TEM images (Figure 5d). In a kinetically favored state, the UV-induced termination of the self-assembly of PDI-DA is a result of the formation of a conjugated ene-yne backbone structure. The covalent bonds linked between adjacent molecules effectively prevent the dissociation of metastable self-assembled structures. In particular, UV irradiation on nanoparticles prevents the conversion from H-aggregate to J-aggregate. In order to get insight into the formation of the PDA backbone, Raman spectroscopic analyses were carried out (Figure S8, Supporting Information). Raman spectra of monomeric PDI-DA fibers of J-aggregate assembly showed the acetylene band at 2269 cm⁻¹. Upon UV-irradiation, the diacetylene band corresponding to the monomeric form disappeared and a characteristic band for the conjugated ene-yne backbone of PDA appeared at 2098 cm⁻¹ and 2269 cm⁻¹. Similarly, UV-

induced polymerization was attempted for nanoparticles of PDI-DA, which displayed a conjugated ene-yne band appearing at 2098 cm⁻¹ (C≡C) and 1467 cm⁻¹ (C=C). However, the weak polymer peaks in nanoparticles indicate the formation of a relatively shorter PDA backbone after UV exposure in kinetically preferred metastable intermediates. This suggests that PDI-DA has lower packing and poor spatial arrangement of DA moieties in the H-aggregate state than J-aggregate.

The polymerized fibrous PDI-DA displays phase-dependent distinctive chromatic and fluorescence behaviors. The transformation of monomeric PDI-DA nanofibers (J-aggregates) into PDA nanofibers was monitored by UV absorption spectroscopy (Figure S9, Supporting Information). As can be seen in **Figure 6**a,b, the monomeric PDI-DA fibers appear red with strong red-phase fluorescent, and the polymerization of red-phase monomeric PDI-DA fibers proceeded with fluorescence quenching to generate a purple-phase PDI-PDA. Since the polymerized PDI-DA absorbs visible light, fluorescence quenching behavior is expected due to fluorescence resonance energy transfer (FRET) between emissive PDI fluorophore and the conjugated PDA acceptor. The FRET phenomenon is also confirmed by absorption and emission spectroscopy and a spectral overlapping pattern is displayed in Figure 6c. The blue line in Figure 6c represents the absorption spectrum of purple phase PDA of PDI-DA fibers appearing at 615 nm. This was obtained by subtracting the absorption spectrum of monomer fibers from polymer fibers (Figure S9, Supporting Information). The monomer PDI-DA shows emission at 620 nm from the PDI fluorophore when excited at 375 nm (dashed line). It
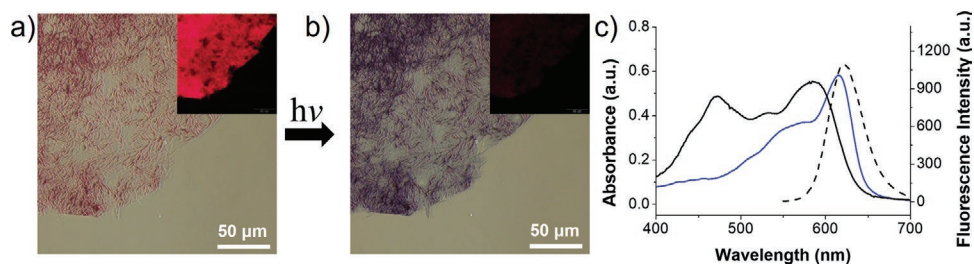
Figure 6. a,b) Optical and fluorescence (λ_{ex} = 520–560 nm, inset images) microscope images of PDI-DA fiber on a glass substrate. PDA formed by UV irradiation (20 mW cm^{-2}) of PDI-PDA fiber for 60 s. c) Förster resonance energy transfer (FRET) process. Spectral overlap between UV-vis absorption of polymerized PDI-PDA nanofibers (blue line) and fluorescence emission of monomer PDI-DA nanofibers (dashed line). Black line represent UV-vis absorption of monomer PDI-DA nanofiber.

can be seen in Figure 6c that the absorption band of the purple phase PDA overlaps with the emission spectrum of PDI fibers and the FRET phenomenon occurs.

An interesting result was observed that the polymerized PDI-DA fibers exhibited reversible thermochromism (**Figure 7**a,b). The purple phase polymeric PDI-PDA fibers turn red color upon heating to 70 °C and the purple phase PDA was recovered completely during the reversible cooling cycle. In the experiment, the heating-cooling process was performed while polymer fibers were dispersed in the solvent mixture. Interestingly, the heat-treated red phase PDA fibers displayed fluorescent character (image inset in Figure 7a,b). However, the absorption spectrum of red phase PDA (red line) and the emission spectrum of PDI-DA (dashed line) did not overlap (Figure 7c), which indicates the FRET phenomena

did not occur during the heating cycle and the PDA fibers have low fluorescence intensity compared to initial unpolymerized fibers. The reversible transformation between purple-phase PDA and red-phase PDA was also observed in the UV-vis absorption spectrum (Figure 7d). UV-vis spectra also assist in the assignment of transformation of J-aggregate into H-aggregate in the transient absorption spectra. (Figure 7d). As J-aggregate transformed to H-aggregates, the characteristic absorption band of J-aggregates disappears. Since H-aggregates have a relatively large overlap between PDI molecules, the heat-treated polymer fibers have low fluorescence intensity. This observation shows that strong π-π stacking and hydrogen bonding not only generate reversible thermochromism of PDA but also cause the reversible conversion of J- and H-aggregate.
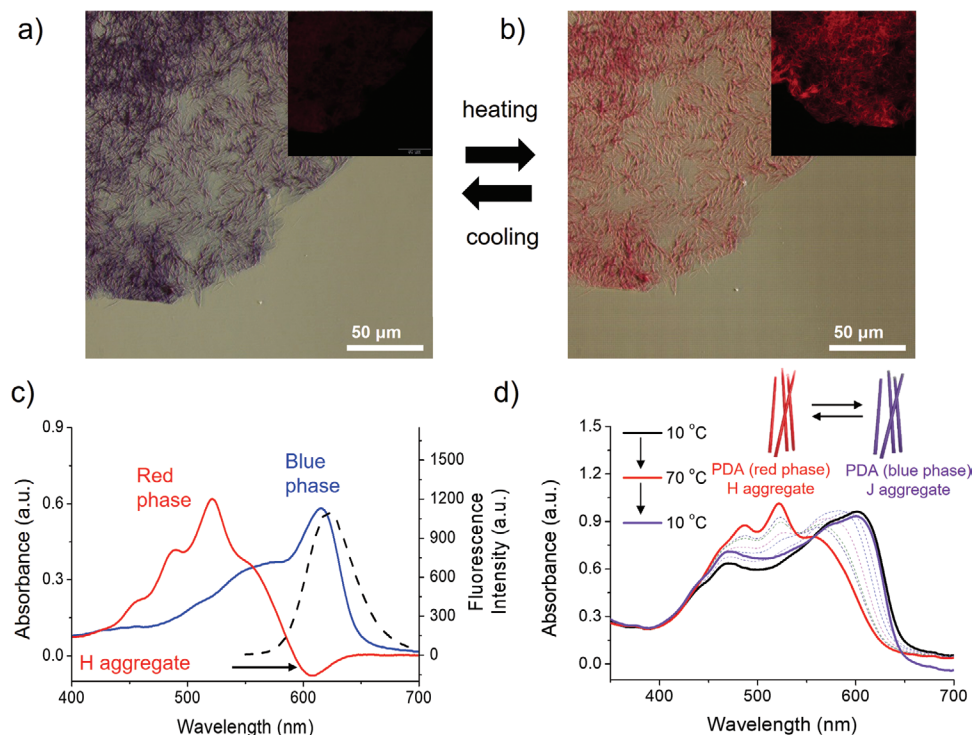

Figure 7. a,b) Optical and fluorescence microscope images (λ_{ex}=520-560 nm) of PDI-PDA fiber on a glass substrate during heating-cooling cycles. c) Temperature-dependent absorption spectral changes of polymerized H-aggregates (red line) and J-aggregates (black, purple line) in Tol/MCH (1:3, v/v). (c) overlap between UV-vis absorption of polymerized purple phase PDI-PDA nanofibers (blue line) and fluorescence emission of monomer PDI-DA nanofibers (dashed line). Red line represents UV-vis absorption of heat-treated red phase PDI-PDA nanofiber.

3. Conclusion

In conclusion, the findings from the described experiments provide detailed insight into the mechanism of the self-assembly process and pathway complexity in π-electron-rich supramolecule. A novel π-electron-rich PDI-DA/PDA having symmetrical DA chains to the PDI is described. The PDI-DA displayed a temperature-dependent self-assembly behavior and distinct morphology corresponding to the kinetic and thermodynamic self-assembly pathway. To understand the self-assembly pathways, a strategy of UV-induced polymerization was adopted to trap and capture metastable kinetic intermediates to understand the self-assembly. Morphological investigation using transmission electron microscopy revealed the existence of two kinetic products at varying temperatures with nanosheet and nanoparticle morphology. The morphological transformation during the self-assembly process is arrested by an effective exposure to the UV light, which triggers the topochemical polymerization of stacking DA units forming a covalently connected PDA backbone. The robust PDA backbone ensures a clamping force to preserve the morphology of the kinetic product. On the other hand, the thermodynamic pathway generated fibrous morphology for the self-assembled PDI-DA. UV-vis spectroscopic experiments revealed that revealed the existence of distinct H- and J-aggregates for kinetic and thermodynamic products respectively. In addition, the polymerized PDI-DA fibers displayed a reversible thermochromic behavior during an alternate heating-cooling cycle with the chromatic transition between the purple (cooling) and red (heat) phase. The chromatic reversibility is accompanied by switching between J-aggregate and H-aggregate, and alternate fluorescence switching features.

The study of these insights is necessary to understand the mechanistic pathway, particularly the strategy of UV-induced polymerization to trap and preserve the intermediate products gives information on the kinetic pathway involved in the ultimate construction of optimized functional materials.

Supporting Information

Supporting Information is available from the Wiley Online Library or from the author.

Conflict of Interest

The authors declare no conflict of interest.

Data Availability Statement

The data that support the findings of this study are available from the corresponding author upon reasonable request.

[1] E. Busseron, Y. Ruff, E. Moulin, N. Giuseppone, *Nanoscale* **2013**, *5*, 7098.

[2] T. Chen, M. Li, J. Liu, *Cryst. Growth Des.* **2018**, *18*, 2765.

[3] B. O. Okesola, Y. Wu, B. Derkus, S. Gani, D. Wu, D. Knani, D. K. Smith, D. J. Adams, A. Mata, *Chem. Mater.* **2019**, *31*, 7883.

[4] A. J. Savyasachi, O. Kotova, S. Shanmugaraju, S. J. Bradberry, G. M. Ó'Máille, T. Gunnlaugsson, *Chem* **2017**, *3*, 764.

[5] H. W. Schmidt, F. Wurthner, *Angew. Chem., Int. Ed.* **2020**, *59*, 8766.

[6] K. Ariga, X. Jia, J. Song, J. P. Hill, D. T. Leong, Y. Jia, J. Li, *Angew. Chem., Int. Ed.* **2020**, *59*, 15424.

[7] Y. Dorca, R. Sánchez-Naya, J. Cerdá, J. Calbo, J. Aragó, R. Gómez, E. Ortí, L. Sánchez, *Chem. - Eur. J.* **2020**, *26*, 14700.

[8] L. Li, R. Sun, R. Zheng, *Mater. Des.* **2021**, *197*, 109209.

[9] V. Palermo, P. Samori, *Angew. Chem., Int. Ed.* **2007**, *46*, 4428.

[10] T. Yokoyama, S. Yokoyama, T. Kamikado, Y. Okuno, S. Mashiko, *Nature* **2001**, *413*, 619.

[11] S. Samanta, P. Raval, G. N. M. Reddy, D. Chaudhuri, *ACS Cent. Sci.* **2021**, *7*, 1391.

[12] A. S. Mahadevi, G. N. Sastry, *Chem. Rev.* **2016**, *116*, 2775.

[13] W. Liu, Q.-Q. Wang, Y. Wang, Z.-T. Huang, D.-X. Wang, *RSC Adv.* **2014**, *4*, 9339.

[14] Q. Li, C. Han, S. R. Horton, M. Fuentes-Cabrera, B. G. Sumpter, W. Lu, J. Bernholc, P. Maksymovych, M. Pan, *ACS Nano* **2012**, *6*, 566.

[15] P. A. Korevaar, C. Grenier, A. J. Markvoort, A. P. H. J. Schenning, T. F. A. de Greef, E. W. Meijer, *Proc. Natl. Acad. Sci. U. S. A.* **2013**, *110*, 17205.

[16] R. Li, M. Boyd-Moss, B. Long, A. Martel, A. Parnell, A. J. C. Dennison, C. J. Barrow, D. R. Nisbet, R. J. Williams, *Sci. Rep.* **2017**, *7*, 4797.

[17] G. Ouyang, M. Liu, *Mater. Chem. Front.* **2020**, *4*, 155.

[18] J. Rottler, M. Müller, *ACS Nano* **2020**, *14*, 13986.

[19] M. F. J. Mabesoone, A. J. Markvoort, M. Banno, T. Yamaguchi, F. Helmich, Y. Naito, E. Yashima, A. R. A. Palmans, E. W. Meijer, *J. Am. Chem. Soc.* **2018**, *140*, 7810.

[20] P. A. Korevaar, T. F. A. de Greef, E. W. Meijer, *Chem. Mater.* **2014**, *26*, 576.

[21] E. E. Greciano, B. Matarranz, L. Sánchez, *Angew. Chem., Int. Ed.* **2018**, *57*, 4697.

[22] P. A. Korevaar, S. J. George, A. J. Markvoort, M. M. J. Smulders, P. A. J. Hilbers, A. P. H. J. Schenning, T. F. A. De Greef, E. W. Meijer, *Nature* **2012**, *481*, 492.

[23] D. van der Zwaag, P. A. Pieters, P. A. Korevaar, A. J. Markvoort, A. J. H. Spiering, T. F. A. de Greef, E. W. Meijer, *J. Am. Chem. Soc.* **2015**, *137*, 12677.

[24] T. Yumura, W. Yamamoto, *J. Phys. Chem. C* **2018**, *122*, 18151.

[25] A. Trubiano, M. Holmes-Cerfon, *Soft Matter* **2021**, *17*, 6797.

[26] I. Robayo-Molina, A. F. Molina-Osorio, L. Guinane, S. A. M. Tofail, M. D. Scanlon, *J. Am. Chem. Soc.* **2021**, *143*, 9060.

[27] J. Matern, Y. Dorca, L. Sánchez, G. Fernández, *Angew. Chem., Int. Ed.* **2019**, *58*, 16730.

[28] J. Seo, J. F. Joung, S. Park, Y. J. Son, J. Noh, J.-M. Kim, *Nat. Commun.* **2020**, *11*, 6260.

[29] L. R. MacFarlane, H. Shaikh, J. D. Garcia-Hernandez, M. Vespa, T. Fukui, I. Manners, *Nat. Rev. Mater.* **2021**, *6*, 7.

[30] Y. Li, X. Zhang, D. Liu, *J. Photochem. Photobiol. C: Photochem. Rev.* **2021**, *48*, 100436.

[31] F. J. M. Hoeben, P. Jonkheijm, E. W. Meijer, A. P. H. J. Schenning, *Chem. Rev.* **2005**, *105*, 1491.

[32] T. Aida, E. W. Meijer, S. I. Stupp, *Science* **2012**, *335*, 813.

[33] S. Chen, P. Slattum, C. Y. Wang, L. Zang, *Chem. Rev.* **2015**, *115*, 11967.

[34] X. Ma, Y. Zhang, Y. Zhang, C. Peng, Y. Che, J. Zhao, *Adv. Mater.* **2015**, *27*, 7746.

[35] G. Wegner, *Makromol. Chem.* **1972**, *154*, 35.

[36] M. N. Tahir, A. Nyayachavadi, J.-F. Morin, S. Rondeau-Gagné, *Polym. Chem.* **2018**, *9*, 3019.

[37] Y. Xu, G. Yang, H. Xia, G. Zou, Q. Zhang, J. Gao, *Nat. Commun.* **2014**, *5*, 5050.

[38] G. Wang, Y. Li, X. Huang, D. Chen, *Polym. Chem.* **2021**, *12*, 3257.

[39] D. Seo, T. C. Major, D. H. Kang, S. Seo, K. Lee, R. H. Bartlett, J. Kim, *ACS Sens.* **2021**, *6*, 3170.

[40] M. Nakamitsu, H. Imai, Y. Oaki, *ACS Sens.* **2020**, *5*, 133.

[41] M. Nakamitsu, K. Oyama, H. Imai, S. Fujii, Y. Oaki, *Adv. Mater.* **2021**, *33*, 2008755.

[42] M. Weston, A. D. Tjandra, R. Chandrawati, *Polym. Chem.* **2020**, *11*, 166.

[43] S. Lee, J.-Y. Kim, X. Chen, J. Yoon, *Chem. Commun.* **2016**, *52*, 9178.

[44] Y. K. Choi, S. Y. Lee, D. J. Ahn, *J. Mater. Chem. C* **2019**, *7*, 13130.

[45] R. Israeli, S. Kolusheva, P. Mateos-Gil, E. Gizeli, R. Jelinek, *ACS Appl. Polym. Mater.* **2021**, *3*, 2931.

[46] V. K. Rao, N. Shauloff, X. Sui, H. D. Wagner, R. Jelinek, *J. Mater. Chem. C* **2020**, *8*, 6034.

[47] I. J. Martin, K.-C. Shih, M.-P. Nieh, R. M. Kasi, *Macromolecules* **2020**, *53*, 4501.

[48] J. Lee, H. T. Chang, H. An, S. Ahn, J. Shim, J.-M. Kim, *Nat. Commun.* **2013**, *4*, 2461.

[49] J. Park, J.-M. Heo, S. Seong, J. Noh, J.-M. Kim, *Nat. Commun.* **2021**, *12*, 4207.

[50] J.-M. Heo, Y. Kim, S. Han, J. F. Joung, S. Lee, S. Han, J. Noh, J. Kim, S. Park, H. Lee, Y. M. Choi, Y.-S. Jung, J.-M. Kim, *Macromolecules* **2017**, *50*, 900.

[51] D. Jang, J.-M. Heo, F. Jannah, M. I. Khazi, Y. J. Son, J. Noh, H. An, S. M. Park, D. K. Yoon, N. N. Kadamannil, R. Jelinek, J.-M. Kim, *Angew. Chem., Int. Ed.* **2022**, *61*, e202211465.

[52] W. Wagner, M. Wehner, V. Stepanenko, S. Ogi, F. Würthner, *Angew. Chem., Int. Ed.* **2017**, *56*, 16008.